







# Ex Vivo Functional Characterization of Mouse Olfactory Bulb Projection Neurons Reveals a Heterogeneous Continuum

 Sana Gadiwalla,<sup>1,2</sup>  Chloé Guillaume,<sup>1</sup>  Li Huang,<sup>1</sup> Samuel J. B. White,<sup>1</sup>  
 Nihal Basha,<sup>1</sup>  Pétur Henry Petersen,<sup>2</sup> and  Elisa Galliano<sup>1</sup>

<sup>1</sup>Department of Physiology, Development and Neuroscience, University of Cambridge, Cambridge CB23EL, United Kingdom and <sup>2</sup>Department of Anatomy, Biomedical Center, Faculty of Medicine, University of Iceland, Reykjavik 102, Iceland

## Abstract

Mitral cells (MCs) and tufted cells (TCs) in the olfactory bulb (OB) act as an input convergence hub and transmit information to higher olfactory areas. Since first characterized, they have been classed as distinct projection neurons based on size and location: laminarily arranged MCs with a diameter larger than 20  $\mu\text{m}$  in the mitral layer (ML) and smaller TCs spread across both the ML and external plexiform layers (EPL). Recent *in vivo* work has shown that these neurons encode complementary olfactory information, akin to parallel channels in other sensory systems. Yet, many *ex vivo* studies still collapse them into a single class, mitral/tufted, when describing their physiological properties and impact on circuit function. Using immunohistochemistry and whole-cell patch-clamp electrophysiology in fixed or acute slices from adult mice, we attempted to align *in vivo* and *ex vivo* data and test a soma size-based classifier of bulbar projection neurons using passive and intrinsic firing properties. We found that there is no clear separation between cell types based on passive or active properties. Rather, there is a heterogeneous continuum with three loosely clustered subgroups: TCs in the EPL, and putative tufted or putative MCs in the ML. These findings illustrate the large functional heterogeneity present within the OB projection neurons and complement existing literature highlighting how heterogeneity in sensory systems is preponderant and possibly used in the OB to decode complex olfactory information.

*Key words:* axon initial segment; excitability; mitral cells; olfactory bulb; parallel processing; tufted cells

## Significance Statement

Mitral cells (MCs) and tufted cells (TCs) in the olfactory bulb (OB) have traditionally been either grouped due to their shared role in early odor processing or separated into distinct groups based on *in vivo* physiology and circuit connectivity. However, our *ex vivo* study in postweaning mice reveals a more complex picture. Rather than being clearly distinct or identical, MCs and TCs form a diverse continuum of morphological and functional properties. This variability may enable efficient processing of the wide range of odors animals encounter. These findings highlight the importance of considering nuanced differences when classifying neurons in the OB and more broadly in the brain.

## Introduction

To guide behavior, concurrent and complex information from the environment must be efficiently decoded and processed by parallel pathways. First described for nociception and vision, parallel processing is now recognized as a hallmark strategy of the brain across sensory systems (Gasser and Erlanger, 1929; Hubel and Wiesel, 1959; Nassi and Callaway, 2009). In the mammalian olfactory system, parallel processing is implemented

Received Sept. 17, 2024; revised Jan. 6, 2025; accepted Jan. 10, 2025.

The authors declare no competing financial interests.

Author contributions: S.G., P.H.P., and E.G. designed research; S.G., C.G., L.H., and S.J.B.W. performed research; S.J.B.W. contributed unpublished reagents/analytic tools; S.G., C.G., L.H., N.B., and E.G. analyzed data; S.G. and E.G. wrote the paper.

We thank Sue Jones, Matthew Grubb, and Ailie McWhinnie for their comments on the manuscript and all members of the Galliano Laboratory for providing helpful discussions.

*Continued on next page.*

via two classes of output neurons, mitral cells (MCs) and tufted cells (TCs), which bring odor information transduced in the olfactory epithelium and preprocessed in the olfactory bulb (OB) to higher olfactory areas. While often lumped together and collectively referred to as mitral/tufted cells (M/TCs), recent work has started to highlight that these two classes of projection neurons are rather different.

MCs are laminarily arranged in the mitral layer (ML) and are known to have the largest somatic diameter (>20  $\mu\text{m}$ ) in the main OB (Nagayama et al., 2014; Imamura et al., 2020). Conversely, TCs are diffusely located throughout the external plexiform layer (EPL). TCs are further subdivided into groups based on their soma position: superficial, middle, internal/deep, and from closest to furthest from the glomerular layer (GL), respectively (Schneider and Macrides, 1978; Orna et al., 1984; Nagayama et al., 2014). It should be noted that internal TCs are sometimes called “displaced MCs” due to their proximity to the ML (Mori et al., 1983; Ma et al., 2013). The TC soma diameter ranges between 10 and 20  $\mu\text{m}$  and is not correlated to their EPL location (Pinching and Powell, 1971; Fukunaga et al., 2012; Nagayama et al., 2014).

Beyond the soma size, MCs and TCs are very similar morphologically, both having a primary apical dendrite which ends with a tuft into a single glomerulus (Pinching and Powell, 1971). However, they are differentially connected within the OB network, and superficial TCs receive stronger excitatory inputs from olfactory sensory neurons (OSNs) than MCs (Jones et al., 2020), as well as inhibitory drive from interneurons in the glomerular and granular layers (Christie et al., 2001; Geramita et al., 2016; Liu et al., 2019). Additionally, in higher olfactory areas, MCs reach wider territories of the piriform cortex (Nagayama, 2010; Igarashi et al., 2012), a difference recapitulated at the molecular level by a differential expression of axon guidance genes (Zeppilli et al., 2021).

Functionally, *in vivo* studies have shown that MCs and TCs encode complementary information thanks to different biophysical characteristics (Balu et al., 2004; Nagayama et al., 2004; Padmanabhan and Urban, 2010; Angelo and Margrie, 2011; Burton and Urban, 2014; Cavarretta et al., 2018; Ackels et al., 2020). Specifically, MCs encode odor concentration, while TCs play a key role in odor discrimination (Fukunaga et al., 2012; Igarashi et al., 2012; Burton and Urban, 2014; Nagayama et al., 2014, but see Chae et al., 2022). As such, TCs exhibit greater firing rates than MCs and have a shorter latency for odor response (Nagayama et al., 2004; Igarashi et al., 2012; Ackels et al., 2020).

Yet, despite this substantial *in vivo* evidence of diversity, few *ex vivo* studies discriminate between MCs and TCs and instead collapse them into an M/TC group. This lack of specificity between OB projection neurons, which is somewhat unsurprising given that the generation of specific transgenic mouse lines is very recent (Koldaeva et al., 2021), makes it difficult to align results across studies. A decade ago, Burton and Urban started to fill this gap by showing how internal TCs substantially differ from very large neurons in the ML (putative MCs, pMCs) in preweaning mice (Burton and Urban, 2014). This seminal study left three important questions unanswered: (1) whether the 20- $\mu\text{m}$ -diameter classifier often used maps onto their data, (2) whether smaller cells in the ML are more similar to EPL TCs or to MCs, and (3) whether their results persist in adult animals given that in the first postnatal weeks, both TCs and MCs are still undergoing developmental changes (Yu et al., 2015; Tufo et al., 2022). To answer these questions and to harmonize recent *in vivo* studies with *ex vivo* work performed in mouse lines without a specific fluorescent tag for MCs or TCs, this study aims to uncover whether the 20- $\mu\text{m}$ -diameter classifier coupled with the intrinsic physiological features of OB projection neurons is sufficient to unequivocally classify MCs and TCs across all layers.

## Materials and Methods

**Animals.** Mice of either sex are housed under a 12 h light/dark cycle in an environmentally controlled room with *ad libitum* access to food and water. In line with the 3R principles, we used both wild-type mice (C57Bl/6J; Charles River Laboratories) and surplus animals from transgenic breedings [DAT<sup>iresCre</sup> (B6.SJL-Slc6a3<sup>tm1.1(cre)Bkmn</sup>/J, Jax stock #006660) and Ai9 [B6.Cg Gt(ROSA)26Sor<sup>tm9(CAG-tdTomato)Hze</sup>/J; Jax stock #007909]] ongoing in the laboratory. Similarly, while almost all mice were postweaning juveniles aged between Postnatal Day (P)20 and P40, for electrophysiology experiments, we also included 7 cells out of a total of 92 (7.6% total, of which 6pMC and 1 eplTC) from mice aged P43, P44, P53, and P68, after confirming the lack of properties of clustering based on age. The integrity of the transgenic lines was ensured by generating breeders via back-

This work was supported by a UKRI Medical Research Council Equipment Grant (MC\_PC\_MR/X012271/1) and project grants from the Royal Society (RGS\R1\19148), the URKI Biotechnology and Biological Sciences Research Council (BB\W014688\1), and the Newton Trust (EG); an Icelandic Research Fund Project Grant 217945-051 (PHP,EG); a Cambridge Trust PhD studentship (LH); and a University of Cambridge Institute of Neuroscience postgraduate scholarship (S.J.B.W.).

Correspondence should be addressed to Elisa Galliano at eg542@cam.ac.uk.

Copyright © 2025 Gadiwalla et al. This is an open-access article distributed under the terms of the Creative Commons Attribution 4.0 International license, which permits unrestricted use, distribution and reproduction in any medium provided that the original work is properly attributed.

crossing heterozygous carriers with C57Bl6 animals specifically bought biannually from Charles Rivers Laboratories. All experiments were performed at the University of Cambridge in accordance with the Animals (Scientific procedures) Act 1986 and with AWERB (Animal Welfare and Ethical Review Board) approval.

**Immunohistochemistry.** Mice were anesthetized with a lethal dose of pentobarbital and perfused with 20 ml PBS with heparin (20 ml units.ml<sup>-1</sup>), followed by 20 ml of 1% paraformaldehyde (PFA; in 3% sucrose, 60 mM PIPES, 25 mM HEPES, 5 mM EGTA, and 1 mM MgCl<sub>2</sub>). OBs were dissected and postfixed in 1% PFA for 2–7 d and embedded in 5% agarose and sectioned into 50 μm slices using a vibratome (VT1000S, Leica Biosystems). Free-floating slices were washed with PBS and incubated in 5% normal goat serum in PBS/Triton X-100/azide (0.25% Triton X-100, 0.02% azide) for 2 h at room temperature and then incubated in primary antibody solution (in PBS/Triton X-100/azide) for 2 d at 4°C. Primary antibodies and their working dilutions included SMI-32 neurofilament H nonphosphorylated (SMI-32; mouse, BioLegend; 1:1,000), ankyrin-G (AnkG; guinea pig, Synaptic Systems, 1:500), and tyrosine hydroxylase (TH; rabbit, Sigma Millipore AB152, 1:500). Following primary incubation, slices were washed three times in PBS for 5 min before secondary antibody solution (species-appropriate, Life Technologies, Alexa Fluor-conjugated) 1:1,000 in PBS/Triton X-100/azide for 3 h at room temperature. Slices were then washed in PBS and incubated in 0.2% Sudan black in 70% ethanol at room temperature for 3 min to minimize autofluorescence and mounted on glass slides (Menzel-Gläser) with FluorSave (Merck Millipore).

**Fixed tissue imaging and analysis.** Images were acquired with a laser scanning confocal microscope (Carl Zeiss LSM 900) using appropriate excitation and emission filters, a pinhole of 1 AU, and a 40× oil immersion objective. Laser power and gain were set to prevent signal saturation in channel images for localization analysis. All quantitative analysis was performed with Fiji (ImageJ). We identified M/TCs with antibodies against the neurofilament marker protein, SMI-32, which labels the cell body, axon, and dendrites of bulbar excitatory neurons. To unequivocally define the upper border of the EPL, we costained the tissue with antibodies against TH to label GL's dopaminergic neurons (Fig. 1A). For soma size analysis, images were taken with a 1× zoom (0.415 μm/pixel) and 512 × 512 pixels in z-stacks with 1 μm steps. In all animals, images were sampled from the rostral third, middle third, and caudal third of the OB. To avoid selection bias, all cells present in the stack and positive for the SMI-32 were measured using Fiji/ImageJ. Soma area, Feret's diameter (i.e., the longest distance between any two points), roundness ( $4 * \text{area} / (\pi * \text{major axis}^2)$ ), and circularity ( $4\pi * \text{area} / \text{perimeter}^2$ ) were measured at the single plane including the cell's maximum diameter by drawing an ROI with the freehand drawing tool. Cells were classified based on their location within the ML and EPL. If their soma fell clearly within the boundaries of the ML, it was determined to be a putative mitral or TC. Alternatively, neurons whose soma was fully located in lower third of the EPL (i.e., the EPL third closest to the ML) were classed as EPL TCs.

For axon initial segment identification, images were taken with 2× zoom, 512 × 512 pixels (0.138 μm/pixel) in z-stacks with 0.30 μm steps. Laser power and gain settings were adjusted to prevent signal saturation in the axon initial segment label AnkG. The cellular marker SMI-32 signal which labels tufted excitatory neurons (Hamada et al., 2016; Galliano et al., 2021) was usually saturated to enable clear delineation of the axon. Distance from soma and length was measured in Fiji/ImageJ using the View5D plugin which allows for 3D manual tracing of cell processes. The axon initial segment distance from soma was calculated as the neurite path distance between its start (proximal part where AnkG staining was clearly identifiable) and the start of its primary parent process (the axon). Axon initial segment length was calculated by following AnkG staining along the course of the axon from the AIS start position to the point where AnkG staining was no longer identifiable and only SMI-32 staining was present along the axon.

**Electrophysiology.** Mice were decapitated under isoflurane anesthesia. The brain was removed and transferred into ice-cold slicing medium containing the following (in mM): 240 sucrose, 5 KCl, 1.25 NaH<sub>2</sub>PO<sub>4</sub>, 2 MgSO<sub>4</sub>, 1 CaCl<sub>2</sub>, 26 NaHCO<sub>3</sub>, and 10 D-glucose, bubbled with 95% O<sub>2</sub> and 5% CO<sub>2</sub>. Horizontal slices (300 μm) of the OB were cut using a vibratome (Campden Instruments 7000SMZ-2 or Leica VT1000S) and stored in ACSF containing the following (in mM): 124 NaCl, 2.5 KCl, 1.25 NaH<sub>2</sub>PO<sub>4</sub>, 2 MgSO<sub>4</sub>, 2 CaCl<sub>2</sub>, 26 NaHCO<sub>3</sub>, and 15 D-glucose, bubbled with 95% O<sub>2</sub> and 5% CO<sub>2</sub> for at least 1 h at room temperature before experiments began.

Cells were visualized with an upright microscope (BX51W1; Olympus) using a 40× water immersion objective with a visible light camera (quantalux sCMOS; Thorlabs) and classified based on their location in the MCL and EPL. Cells were targeted for patch clamp if the entirety or over half of their soma lay between the boundaries of the MCL and had a max diameter >10 μm, i.e., bigger than that of the rare 5T4-expressing MCL granule cells (Batista-Brito et al., 2008). Internal TCs were targeted based on their location in the lower third of the EPL (Mori et al., 1983; Kishi et al., 1984; Shepherd, 2004).

Whole-cell patch-clamp recordings were amplified and digitized using an EPC-9 (HEKA Elektronik) or MultiClamp 700B and Digidata 1550B (Molecular Devices) at physiologically relevant temperatures (30 ± 2°C), maintained with an in-line heater (SH-27B and TC-344C, Warner Instruments). All signals were Bessel filtered at 10 kHz, with experiments recorded at 20 kHz and single-spike recordings filtered at 200 kHz. Recordings were excluded if series resistance (evaluated by –10 mV voltage steps following each test pulse) was <40 MΩ for putative MCs with a capacitance >40 pF and <30 MΩ for putative TCs with a capacitance <40 pF. Protocols were also excluded if these values varied >20% over the course

of the experiment and holding current values exceeded  $-300$  pA. Fast capacitance was compensated in on-cell configuration. Cell capacitance was calculated by measuring the area under the curve of a transient capacitive current induced by a  $-10$  mV step after subtracting the steady-state current induced by the voltage pulse. Recording electrodes (30-0094 and 30-0062, Harvard Apparatus) were pulled using a horizontal or vertical puller (P-87, Sutter Instruments; PC-100, Narishige) to achieve a tip resistance of  $1.5$ – $3.0$  M $\Omega$  (larger tips for putative mitral, smaller for putative tufted and EPL tufted) when filled with a potassium-gluconate intracellular solution containing the following (in mM): 124 K-gluconate, 9 KCl, 10 KOH, 4 NaCl, 10 HEPES, 28.5 sucrose, 4 Na<sub>2</sub>ATP, 0.4 Na<sub>3</sub>GTP, pH 7.25–7.35 (290 MOsm), and Alexa Fluor 488 (Thermo Fisher Scientific, 1:150).

To precisely measure the soma size and ensure fluorophore diffusion throughout the entire soma and confirm that the dendrites were not severely cut, cells were patched for at least 10–15 min prior to capturing a snapshot of their Alexa Fluor 488-filled soma and proximal dendrite (field of view size,  $100.90 \times 179.43$   $\mu\text{m}$ ) with LED excitation (LED1B; Thorlabs) using the appropriate excitation and emission filters (ET575/50 m; CAIRN Research UK). Quantitative analysis was performed in Fiji/ImageJ. Diameter and area were calculated by drawing a ROI using the freehand drawing tool. In a subset of recordings, biocytin (Sigma-Aldrich; 2%) was added to evaluate morphology. These slices were fixed with 1% PFA in PIPES overnight and then incubated with 1:1,000 streptavidin Alexa Fluor 488 conjugate in PBS/Triton X-100/azide for 2 h at room temperature to reveal the biocytin filling.

In a current-clamp mode, experiments were only evaluated if their voltage was maintained stably at  $-60 \pm 3$  mV. For action potential (AP) measurements, injections of 10 ms current steps of increasing amplitudes were applied until current threshold was met, and the cell fired an AP ( $V_{\text{max}} > 0$  mV). Repetitive firing properties were measured with injections of 500 ms current steps starting at 0 mV of increasing amplitudes (5–35) until the neuron passed its maximum firing frequency. Sag potentials were evoked by injecting a 500 ms current injection starting from  $-300$  to  $-700$  pA. Exported traces were analyzed using either ClampFit (pClamp 10, Molecular Devices) or custom-written scripts in MATLAB (MathWorks).

*Quantification of passive and active electrophysiological properties.* Quantification of AP properties was calculated from the first AP evoked by the weakest suprathreshold input. Current threshold was defined as the minimum threshold needed to elicit the first AP. Voltage threshold was taken as the potential at which  $dV/dt$  first passed 10 V/s and the maximum of depolarization. The peak was the highest voltage an AP reached. AP amplitude was the difference between the voltage threshold and the AP peak. Spike width was measured at the midpoint between voltage threshold and maximum voltage. Afterhyperpolarization (AHP) values were measured from responses to 500 ms current injection from the local voltage minimum after the first spike fired at rheobase.

For repetitive firing properties, input–output curves were created by counting the number of spikes fired at each level of injected current density. The slope of the input–output curve was measured between the first sweep with a non-zero AP and the sweep where the maximum number of APs were fired. The following parameters were measured only from the sweep with the maximum number of APs were fired: (1) first AP delay which measured the time interval between the start of the current injection and the peak of the first AP; (2) peak of the first AP; and (3) AP frequency. To measure the variability in the firing pattern, we calculated the coefficient of variance (CV) of the interspike interval (ISI) across current injections and at the sweep that fired the maximum number of APs. CV was calculated as the ratio of the standard deviation of ISIs to the mean ISI of the cell. Firing pattern variability measure CV2 was calculated as mean value of  $(2 * \text{abs}(|\text{ISI}_n + 1 - \text{ISI}_n|) / (\text{ISI}_n + 1 + \text{ISI}_n))$ ; Holt et al., 1996). To further analyze the temporal coding further, we binned the current injection into five 100 ms epochs, and the AP firing was evaluated along them (Goldfarb et al., 2007).

Sag potentials were evaluated as done previously (Angelo and Margrie, 2011) where sag index was calculated as the ratio between the peak (minimum within the first 100 ms) and steady-state (mean of final 50 ms) currents normalized to the holding voltage.

*Statistical analysis and data availability.* Statistical analyses were carried out using Prism (GraphPad) or MATLAB (MathWorks). “ $N$ ” refers to the number of animals, and “ $n$ ” indicates the number of cells. Normality of sample distribution was assessed with the D’Agostino and Pearson’s omnibus test and their parametric or nonparametric tests used accordingly. All comparisons were two-tailed. Multiple comparisons were performed among all groups, and post hoc tests after nested ANOVAs or Kruskal–Wallis were done using Tukey’s/Dunn’s or the two-stage linear step-up false discovery rate (FDR) procedure of Benjamini, Krieger, and Yekutieli. The  $\alpha$  values were set at 0.05, and on the figures only significant differences are indicated with star(s). K-means clustering of immunohistochemistry and electrophysiology data were executed in MATLAB (MathWorks) using custom-written scripts which included an evaluation of silhouette coefficient. Cluster numbers were unbiased, chosen based on the silhouette coefficient closest to one. Principal component analysis (PCA) of electrophysiological data was performed in Prism (GraphPad) for all cells with recordings passing inclusion criteria for all three of these protocols: (1) passive properties, (2) single AP properties, and (3) repetitive firing. Principal components (PCs) were selected based on the Kaiser rule, where PCs were selected only if they had an eigenvalue greater than one. All PCAs were unsupervised. Loading scores were calculated based on standardized data using the following formula:  $[\text{Eigenvector} * \text{sqrt}(\text{Eigenvalue})]$ . Each cell was colored on the plot, post hoc allowing for a visual assessment of

functional clusters. Postpublication, the full dataset will be released on the University of Cambridge Apollo repository (<https://doi.org/10.17863/CAM.114886>) under a CC-BY license.

## Results

### Soma size and morphology of mitral and TCs is heterogeneous

Two criteria have been traditionally used to classify MCs and TCs: the location and size of their somas. There is historical consensus in the literature that MC somas lie entirely or predominantly in the ML and that they are large, with a longest-axis diameter  $>20\ \mu\text{m}$  and a corresponding area  $>350\ \mu\text{m}^2$ . Conversely, TC somas are spread across the EPL and on average smaller than MCs—longest-axis diameter  $<20\ \mu\text{m}$ , area  $<230\ \mu\text{m}^2$  (Mori et al., 1983; Orona et al., 1984; Ezeh et al., 1993; Royet et al., 1998; Nakajima et al., 2001; Shepherd, 2004; Nagai et al., 2005; Fukunaga et al., 2012; Igarashi et al., 2012; Nagayama et al., 2014).

We first investigated whether this historical diameter boundary could be used as a reliable binary classifier of mitral versus tufted identity in the fixed OB tissue. Using confocal microscopy, we acquired 3D z-stacks where we sampled SMI-32-positive neurons in the lower third of the EPL (i.e., internal TCs) and in the ML. We found that TCs in the EPL had a mean diameter of  $15.73\ \mu\text{m}$  and a mean area of  $115.4\ \mu\text{m}^2$  (Fig. 1B, green circles). In the ML, however, we found that soma sizes were more heterogeneous—mean diameter,  $20.61\ \mu\text{m}$ ; range,  $9.46\text{--}39.79\ \mu\text{m}$ ; mean area,  $180.4\ \mu\text{m}^2$ ; range  $19.47\text{--}513.22\ \mu\text{m}^2$  (Fig. 1B, cyan circles; area-diameter linear regression  $R^2 = 0.74$ ; soma diameter frequency distribution; Fig. 1C). To further describe this heterogeneity and given that MCs have been further divided according to soma shape (Kikuta et al., 2013), we calculated the soma roundness at its longest-axis diameter. Smaller cells in the

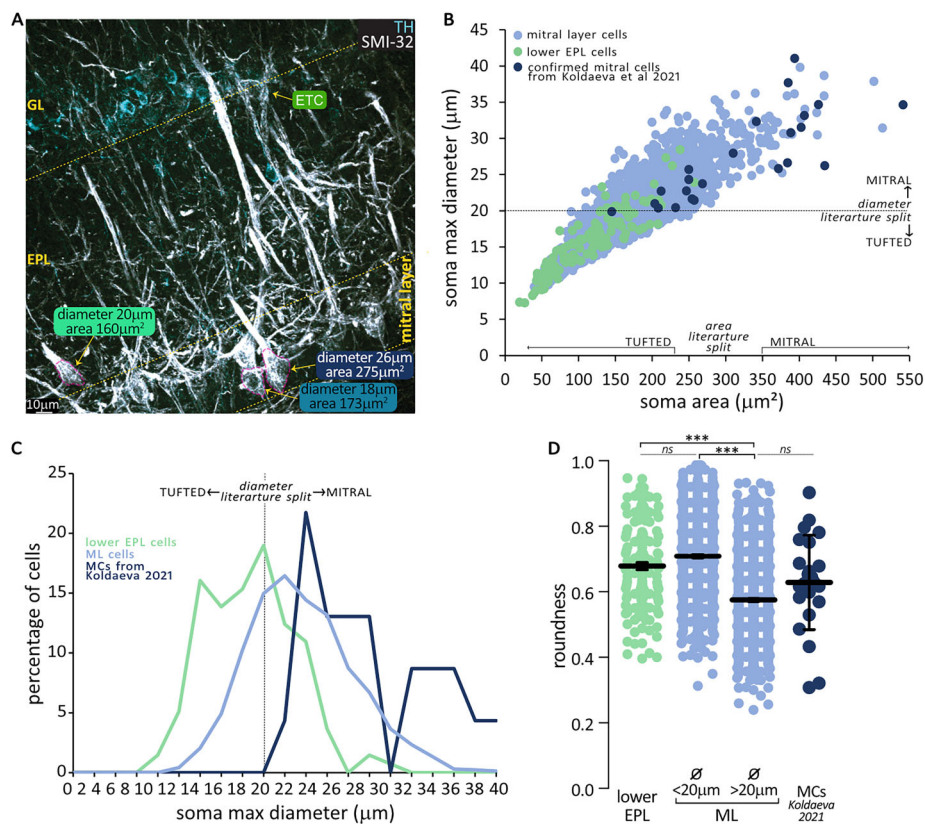


**Figure 1.** OB projection neurons in the ML include differently sized and shaped cells. **A**, An example image of the OB outer layers. Excitatory projection neurons labeled with antibodies against neurofilament marker protein (SMI-32, white) span the EPL and the ML. Dopaminergic interneurons stained with antibodies against TH (cyan) indicate the location of the GL, adjacent to which are the SMI-32 positive somas of the excitatory interneurons external TCs (ETCs). The soma of three representative projection neurons across EPL and ML has been manually traced in dashed magenta to calculate the maximum diameter and area. **B**, Correlation of the soma area and maximum diameter for OB projection neurons located in the lower EPL (green,  $n = 137$ ) or ML (cyan,  $n = 1,671$ ). Blue circles represent confirmed MCs from the Lbhd2-CreERT2 transgenic mouse line, meta-analyzed from Koldaeva et al. 2021 ( $n = 23$ ). The canonical diameter and area dividers between MCs and TCs are indicated on the axes. **C**, Frequency distribution of maximum diameters for OB projection neurons located in the lower EPL (green,  $n = 137$ ), ML (cyan,  $n = 1,671$ ), and confirmed MCs from the Lbhd2-CreERT2 transgenic mouse line. **D**, Soma roundness [ $4 \times \text{area} / (\pi \times \text{major\_axis}^2)$ ] of EPL TCs (green) and confirmed MCs (blue) compared with ML cells (cyan) when split by the  $20\ \mu\text{m}$  max diameter classifier proposed in the literature. Circles are individual cells; lines are mean  $\pm$  SEM; \*\*\* $p < 0.001$ ; ns, not significant.

ML (diameter  $<20\ \mu\text{m}$ ) were rounder than ML cells with a diameter  $>20\ \mu\text{m}$ , but they did not differ in roundness nor in the area from EPL TCs (Kruskal–Wallis with Dunn’s corrections;  $p < 0.0001$ ; Fig. 1D). Moreover, when we performed a secondary analysis of published data in confirmed MCs labeled in the Lbhd2–CreERT2 transgenic mouse line (Koldaeva et al., 2021;  $n = 23$ ; mean diameter,  $27.22\ \mu\text{m}$ ; mean area,  $317.868\ \mu\text{m}^2$ ; mean roundness,  $0.63$ ; Fig. 1B–D, dark blue dots/line), we found that these neurons were similarly sized and shaped as the largest ML cells in our dataset (one-way ANOVA nested on mouse or figure with Tukey’s corrections; roundness  $F_{(3,22)} = 32.95$ ; pMC vs Koldaeva et al., 2021  $p = 0.32$ ; area,  $F_{(3,22)} = 14.90$ ; pMC vs Koldaeva et al., 2021  $p = 0.05$ ; diameter,  $F_{(3,22)} = 16.56$ ; pMC vs Koldaeva et al., 2021  $p = 0.64$ ).

In summary, our data are broadly in agreement with the literature in that TCs in the EPL are round and have on average somas smaller than  $20\ \mu\text{m}$  and that the ML contains some very large and more ovoidal neurons. However, we found no clean split as advocated in previous studies: first, a minority of large soma neurons are present in the EPL, and second, over a third of ML neurons are small and round. These latter cells are more similar in size and shape to EPL TCs than ML MCs, and we tentatively class as putative ML TCs (pTCs).

### Unbiased k-means analysis identifies a capacitance threshold to classify mitral and TCs

Are pTCs in the ML not only morphologically but also physiologically like EPL TCs? To evaluate their electrophysiological properties, we performed whole-cell patch clamp in acute slices, enabling precise determination of soma location (Fig. 2A) and subsequent measurement following intracellular labeling with fluorescent markers (Fig. 2B). Recognizing the well known disparity between live and fixed samples due to fixation-induced tissue shrinkage (Boonstra et al., 1983) and given that our earlier analysis failed to reveal a clear separation using the  $20\text{-}\mu\text{m}$ -diameter classifier in the fixed tissue (Fig. 1B–C), we decided to adopt an alternative classification strategy. To correlate morphology with electrophysiology and ultimately distinguish between pMCs and pTCs based on soma size-related passive properties, we implemented an unbiased  $k$ -means algorithm based on capacitance, a reliable indicator of the somatic size. We input the diameter and capacitance of recorded ML cells into the  $k$ -means algorithm, which yielded two distinct clusters with centroids at  $17.64\ \mu\text{m}$  diameter/ $29.23\ \text{pF}$  capacitance (representing pTCs) and  $22.51\ \mu\text{m}$  diameter/ $61.87\ \text{pF}$  capacitance (representing pMCs). These two clusters could be separated by a capacitance-based classifier of  $45\ \text{pF}$  (Fig. 2C). Using this fully unbiased classifier, we compared mean capacitance of pTCs and pMCs with those of TCs recorded in the EPL ( $41.63 \pm 3.32\ \text{pF}$ ; max diameter,  $18.49 \pm 0.89\ \mu\text{m}$ ) and confirmed that only pMCs are significantly different (Kruskal–Wallis test with Dunn’s corrections epTCs vs pMCs  $p < 0.001$ ; Fig. 2D). In line with this result and in further support of the

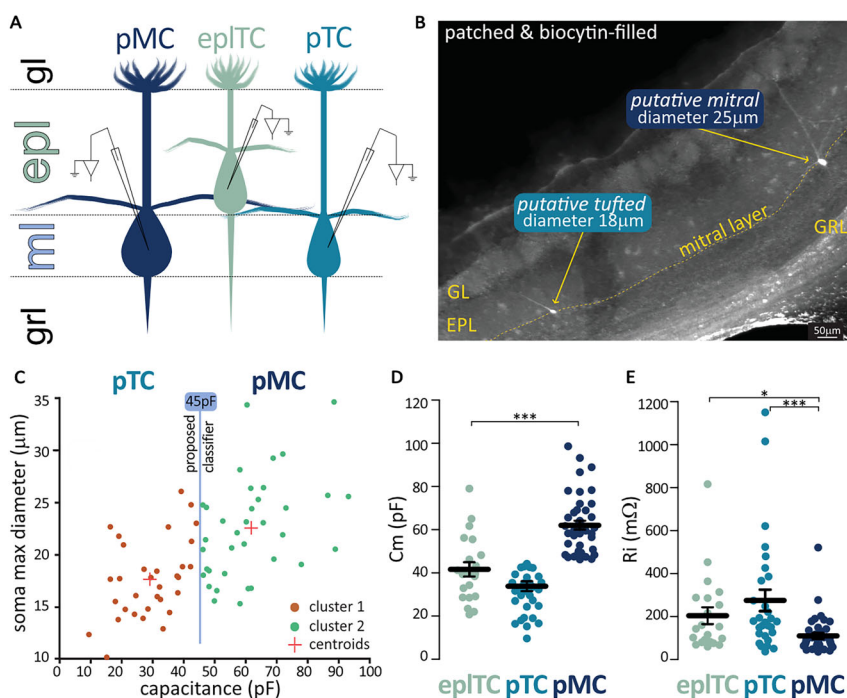


**Figure 2.** The soma size and passive electrical properties differ between OB projection neurons. **A**, Schematic representation of the location of OB projection neurons targeted for whole-cell patch-clamp recordings in acute horizontal mouse brain slices. **B**, Two cells in the ML, a putative tufted (pTC) and a putative mitral cell (pMC) patched with biocytin-supplemented intracellular solution and postfixed for morphological analysis. **C**, Unbiased  $k$ -means analysis of the soma size of patched cells in the ML returns two clusters separable by a  $45\ \text{pF}$  capacitance classifier. **D–E**, Membrane capacitance ( $C_m$ ) and input resistance ( $R_i$ ) in epITC ( $n = 21$ ) and ML’s pTC ( $n = 28$ ) and pMC ( $n = 42$ ) classed using the  $45\ \text{pF}$  divider. Circles are individual cells; lines are mean  $\pm$  SEM; \* $p < 0.05$ ; \*\*\* $p < 0.001$ . GL, glomerular layer; EPL, external plexiform layer; GRL, granule cell layer.

capacitance classifier, we found that input resistance ( $R_i$ , also partially dependent on the soma size) was significantly lower in pMCs than in both pTCs and epITCs (epITC  $205 \pm 39$  m $\Omega$ , pTC  $275 \pm 50$  m $\Omega$ , pMC  $110 \pm 13$  m $\Omega$ ; Kruskal–Wallis test  $p < 0.001$ ; Dunn’s corrections epITCs vs pMCs  $p < 0.05$ ; pTCs vs pMCs  $p < 0.001$ ; Fig. 2E).

In summary, we successfully identified a purely electrophysiological measure—capacitance—that can be used in the live tissue to attempt a classification of ML cells into the two subgroups.

### Sag voltages are not significantly different between principal neurons in EPL and ML

The presence of a hyperpolarization-activated cation current ( $I_h$ /sag currents), which are important determinants of a neuron’s intrinsic excitability (Combe and Gasparini, 2021), have been shown to be variable in ML cells (Angelo and Margrie, 2011; Angelo et al., 2012). To assess if this reported heterogeneity mapped on the pTCs/pMCs subclasses, we injected increasing levels of hyperpolarizing current into ML and EPL principal neurons (Fig. 3A,B). We found no differences between pMCs, pTCs, and epITCs in the raw measurements of sag peak and steady-state voltage nor in the combined measure of sag amplitude and index (Angelo and Margrie, 2011; Fig. 3C–F; ANOVA with Tukey or Kruskal–Wallis with Dunn; all  $p > 0.2$ ; Table 1). Of note is the variability across all groups but especially the pTCs (sag amplitude interquartile range and CV: epITCs, 18.25 mV, –97%; pTCs, 4.4881 mV, –163%; mTCs, 10.48 mV, –174%; sag index interquartile range and CV: epITCs, 0.23 mV, –17%; pTCs, 0.44 mV, –44%; mTCs, 0.13 mV, –21%; Bartlett’s test for equal variances, amplitude  $p < 0.001$ ; index  $p < 0.01$ ). Across all three groups, approximately half of the cells fire on rebound following the hyperpolarization-induced voltage sag (epITCs, 50%; pTCs, 58%; pMCs, 48%;  $\chi^2$  test,  $p = 0.33$ ).

Overall, our data confirm the sag variability reported in the literature, but this heterogeneity does not map onto the pTC and pMC subgroups.

### Higher AP threshold and more distal axon initial segment in epITCs than in ML neurons

Next, we investigated AP threshold and waveform by injecting 10 ms of depolarizing current steps of increasing amplitudes (Fig. 4A). In line with findings from Burton and Urban (2014), the three cell types had similar AP waveforms, with only the peak amplitude being significantly smaller in epITCs (Fig. 4E; Table 1). This difference is in line with similar maximum voltages reached but higher AP threshold in epITC than in ML’s cells (Fig. 4B–D; Table 1). Of note, when the AP threshold is normalized for capacitance, pMCs require smaller injected currents than pTCs to fire (Fig. 4B; Table 1). In contrast to the sodium channel-driven rapid depolarization and in line with molecular data (Zeppilli et al., 2021), the AP phases reliant on potassium conductance (width at half-height, WHH, after-hyperpolarization, AHP) do not differ between the three cell types, except for the higher minimum voltage reached by epITCs (Fig. 4F–H).

In summary, despite being more electronically compact (i.e., able to integrate electrical signals over a smaller spatial area or with fewer/shorter distinct components), epITCs require more current to fire an AP which however has a similar

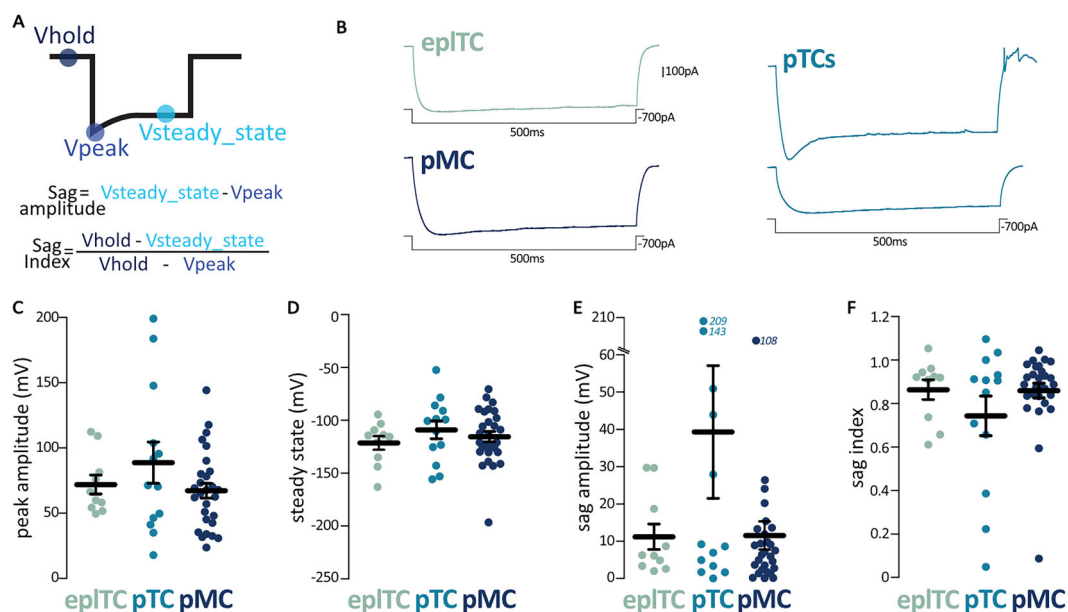


**Figure 3.** The depolarization response to hyperpolarization (sag potential) is extremely variable among OB projection neurons. **A**, Schematic visualization of the voltage sag analysis parameters and formulas used to calculate sag amplitude and index. **B**, Example traces of the voltage sag response to hyperpolarizing current injections in epITC (green,  $n = 10$ ), pTCs (cyan,  $n = 13$ ), and pMC (blue,  $n = 28$ ). Note the variability in pTCs. **C–F**, Peak amplitude, steady-state voltage, sag amplitude, and sag index in the three classes of OB projection neurons. Circles are individual cells; lines are mean  $\pm$  SEM; further quantification and statistical analysis in Table 1.

**Table 1. Intrinsic electrophysiological properties of OB projection neurons**

Intrinsic electrophysiological properties	epITC mean ± SEM, (n)	pTC mean ± SEM, (n)	pMC mean ± SEM, (n)	ANOVA/Kruskal–Wallis <i>p</i> value	Tukey's/Dunn's multiple comparisons <i>p</i> value		
					epITC versus pTC	epITC versus pMC	pTC versus pMC
<b>Sag potentials properties</b>							
Peak amplitude (mV)	71.97 ± 7.24 [10]	88.7 ± 15.82 [13]	67.27 ± 5.63 [28]	A, 0.24 ( <i>F</i> = 1.46)	ns	ns	ns
Steady state (mV)	−121.3 ± 6.5 [10]	−109 ± 8.39 [13]	−115.5 ± 4.89 [28]	KW, 0.52	ns	ns	ns
Sag amplitude (mV)	11.20 ± 3.43 [10]	39.28 ± 17.80 [13]	11.53 ± 3.80 [28]	KW, 0.63	ns	ns	ns
Sag Index	0.86 ± 0.05 [10]	0.74 ± 0.09 [13]	0.86 ± 0.03 [28]	KW, 0.74	ns	ns	ns
<b>APS properties</b>							
Current threshold (pA/pF)	9.63 ± 1.64 [13]	5.46 ± 0.87 [13]	3.06 ± 0.37 [27]	KW, <0.001	ns	***	*
Voltage threshold (mV)	−30.22 ± 2.18 [13]	−37.26 ± 2.76 [13]	−43.14 ± 1.14 [27]	A, <0.001 ( <i>F</i> = 13.14)	ns	***	ns
Maximum voltage (mV)	10.48 ± 2.01 [13]	14.89 ± 2.24 [13]	14.10 ± 1.76 [27]	KW, 0.40	ns	ns	ns
Peak amplitude (mV)	40.17 ± 1.83 [13]	58.56 ± 4.60 [13]	58.29 ± 2.06 [27]	KW, <0.001	**	***	ns
WHH (ms)	0.80 ± 0.08 [13]	0.93 ± 0.06 [13]	0.83 ± 0.03 [27]	KW, 0.25	ns	ns	ns
Minimum voltage (mV)	−46.22 ± 2.05 [15]	−54.03 ± 2.30 [11]	−56.26 ± 1.87 [27]	A, 0.003 ( <i>F</i> = 6.41)	ns	**	ns
AHP on amplitude (mV)	17.13 ± 1.57 [15]	12.61 ± 1.18 [11]	16.59 ± 1.10 [27]	A, 0.08 ( <i>F</i> = 2.58)	ns	ns	ns
<b>Repetitive firing properties</b>							
Rheobase (pA/pF)	3.03 ± 0.69 [14]	1.59 ± 0.29 [11]	1.82 ± 0.31 [28]	A, 0.08 ( <i>F</i> = 2.58)	ns	ns	ns
Slope	7.98 ± 1.38 [13]	6.33 ± 1.24 [11]	7.21 ± 1.01 [26]	A, 0.72 ( <i>F</i> = 0.34)	ns	ns	ns
<b>I/O curve (Hz/pA/pF)</b>							
First AP delay (ms)	109.8 ± 20.6 [15]	169.5 ± 42.1 [11]	161.1 ± 29.1 [27]	KW, 0.78	ns	ns	ns
<i>n</i> APs at rheobase	8.14 ± 2.95 [14]	5.36 ± 1.22 [11]	8.64 ± 2.56 [28]	KW, 0.86	ns	ns	ns
Max number of APs	29.87 ± 4.76 [15]	22.27 ± 3.65 [11]	25.321 ± 2.67 [28]	KW, 0.67	ns	ns	ns
Max frequency (Hz)	110.9 ± 28.1 [15]	131.2 ± 25.4 [11]	80.1 ± 7.3 [28]	KW, 0.19	ns	ns	ns
ISI CV at max firing	0.19 ± 0.03 [14]	0.47 ± 0.16 [11]	0.19 ± 0.02 [27]	KW, 0.20	ns	ns	ns
ISI CV2 at max firing	0.10 ± 0.13 [14]	0.27 ± 0.10 [11]	0.11 ± 0.01 [27]	KW, 0.33	ns	ns	ns

Mean values ± SEM and number of cells (*n*) of sag currents, AP properties, and repetitive firing properties for epITCs and ML's pTCs and pMC. Statistical differences between cell types were calculated independently with a one-way ANOVA with Tukey's post hoc correction for normally distributed data (A) or with a Kruskal–Wallis test with Dunn's post hoc correction for non-normally distributed data (KW). Individual data points and example traces are presented in Figures 3, 4, and 6.

shape to ML cell APs. To investigate whether this threshold difference may be due to morphological differences at the AP initiation site, the axon initial segment (AIS), we performed immunohistochemistry against the AIS master organizer and label AnkG (Fig. 5A; Kole et al., 2007; Bender and Trussell, 2012; Leterrier, 2018; Galliano et al., 2021).

We found no difference in AIS length between the three cell types (epITC, 23.28 ± 1.41 μm; pTC, 23.28 ± 0.80 μm; pMC, 25.07 ± 0.72 μm; ANOVA nested on mouse  $F_{(2,11)} = 0.5529$ ;  $p = 0.59$ ; Fig. 5B,D). Conversely, epITCs' AISes are extremely distal compared with those of principal neurons in the ML (epITC, 21.19 ± 4.78 μm; pTC, 2.88 ± 0.25 μm; pMC, 5.02 ± 0.46 μm; log-transformed data for ANOVA nested on mouse,  $F_{(2,11)} = 14.16$ ;  $p < 0.001$ ; post hoc with FDR correction, epITC vs pTC  $p < 0.001$ ; epITC vs pMC  $p = 0.003$ ; pTC vs pMC  $p = 0.13$ ; Fig. 5C). Recent work has identified axons originating from dendrites not just in inhibitory bulbar interneurons but also in pyramidal cells in the cortex (Galliano et al., 2021; Hodapp et al., 2022), and such dendritic origin can correlate with a more distal AIS location. However, we confirmed that while 8/23 epITCs had dendritic axons, their AISes were not different from the AISes of the 15/23 epITCs in terms of distance from soma, length, or diameter (orange shading in Fig. 5C–D, nested *t* tests; all  $p > 0.09$ ). Importantly, the diameter of both the proximal axon and AIS were identical not just between epITCs with somatic or dendritic-origin AISes, but among all cell types (ANOVA nested on mouse,  $F_{(2,10)} = 1.28$ ;  $p = 0.32$ ;  $F_{(2,10)} = 1.47$ ;  $p = 0.28$ , respectively).

Literature suggests that, at comparable diameters and lengths (Goethals and Brette, 2020), excitability reduces the further the AIS is from the soma as more charge is required to overcome charge dissipation and generate an AP (Yamada and Kuba, 2016). Thus, this morphological data could at least partially explain the higher firing threshold in epITC but fails to account for the difference in firing threshold recorded between pMCs and pTCs in the ML.

**Repetitive AP properties are comparable across putative cell types**

To investigate the rate and temporal coding in projection neurons, we injected longer current steps (500 ms) of increasing intensity (Fig. 6A–D). To account for different cell capacitance, we constructed input–output curves with injected current density as the independent variable (two-way ANOVA; effect of cell type  $F_{(27-220)} = 27.08$ ;  $p = 0.0015$ ; effect of current density  $F_{(14-220)} = 2.24$ ;  $p = 0.07$ ; effect of interaction  $F_{(28-220)} = 2.06$ ;  $p = 0.002$ ; Tukey's multiple comparisons epITC vs pTC  $p = 0.014$ ; epITC vs pMC  $p = 0.16$ ; pTC vs pMC  $p = 0.52$ ; Fig. 6E). From them, we extracted rheobase (Fig. 6F) and the rate



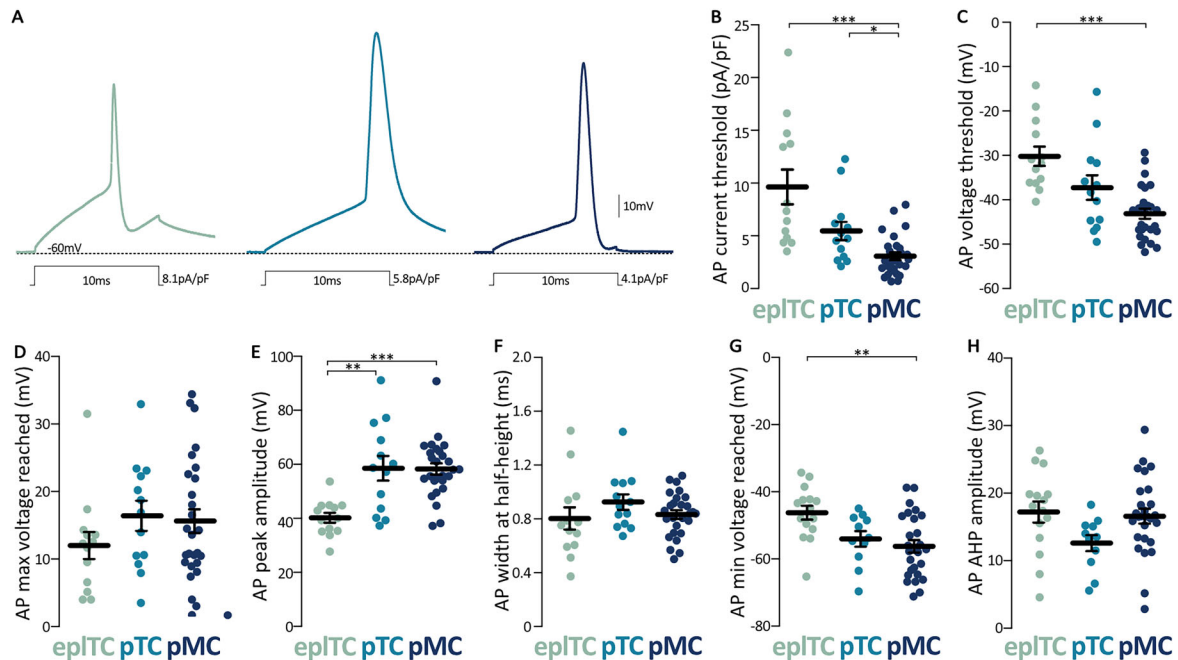


**Figure 4.** AP threshold and waveforms differ between OB projection neurons. **A**, Example traces of the membrane voltage response to the minimum depolarizing 10-ms-long current injection needed to evoke an AP in epITCs (green,  $n = 13$ ), pTCs (cyan,  $n = 13$ ), and pMCs (blue,  $n = 27$ ). Waveform parameters for the three OB projection neurons subtypes include **(B)** injected current density needed to evoke an AP, **(C)** membrane potential at which the AP was evoked, **(D)** maximum voltage reached by the AP, **(E)** AP peak amplitude, **(F)** AP width at half the maximum height, **(G)** minimum voltage reached by the AP, and **(H)** peak amplitude of the AP AHP. Circles are individual cells, lines are mean  $\pm$  SEM; \* $p < 0.05$ ; \*\* $p < 0.01$ ; \*\*\* $p < 0.001$ ; further quantification and statistical analysis in Table 1.

of rise by fitting a line and calculating its slope (Fig. 6G). In line with the current and voltage threshold results discussed above, also with these longer-lasting injections, epITC seemingly took longer than ML cells to fire APs but the rheobase values did not reach significance (Kruskal–Wallis test,  $p = 0.08$ ), and all three cell types had similarly steep input–output relationships (Table 1). We also found no difference between the three cell types in the latency to fire the first AP, in the number of APs threshold or at maximum firing, nor in the maximum AP frequency (Fig. 6H–J; Table 1). Both in vivo and ex vivo preparations have shown that TCs fire more irregularly than MCs (Burton and Urban, 2014; Fourcaud-Trocmé et al., 2022). To investigate firing regularity, we calculated both the ISI CV (where a high ISI CV indicates irregular firing, Fig. 6K) and the CV of adjacent intervals (CV2, sensitive to regularity within a burst; Fig. 6L). Surprisingly, we found no differences between the three cell types in each measure, both at maximum firing (Table 1) and rheobase (data not shown). Moreover, we found that while epITCs are more excitable, all three cell types fire similar number of APs at the beginning, middle, and end of the current injection (bin average AP number two-way ANOVA, effect of cell type  $F_{(2,125)} = 3.58$ ;  $p = 0.03$ ; effect of current density  $F_{(4,125)} = 0.08$ ;  $p = 0.99$ ; effect of interaction  $F_{(8,125)} = 0.05$ ;  $p = 1.00$ ; Fig. 6M). Finally, we checked if the sag voltage amplitude correlated with either firing CV or rheobase (Burton and Urban, 2014) but found a significant correlation only for sag amplitude and rheobase in epITCs (linear regression  $R^2 = 0.054$ ;  $F = 8.22$ ;  $p = 0.02$ ; all other correlations  $p > 0.16$ ; Fig. 6O). Taken together, our results indicate that when capacitance is accounted for, epITCs have similar firing patterns to both pTCs and pMCs in the ML.

### Can putative cell type be accurately classified into discrete groups?

Despite the wealth of literature suggesting that TCs and MCs are physiologically different, our ex vivo data indicate that individual physiological passive and active properties are not sufficient to differentiate them. If individual properties cannot return a clean linear classifier, does the mitral versus tufted split appear when all these values are considered holistically?

To answer this question and determine the source of the variation in our dataset, we performed a PCA including all measurements extracted from passive properties and AP firing protocols (Fig. 7A), after confirming that animal age did not produce distinct clusters (Extended Data Fig. 7-1). The first three PCs cumulatively accounted for 50% of the variance, and the most influential loading scores were connected to AP amplitude and threshold, as well as capacitance (Fig. 7B,C). While on average epITCs and pMCs clustered at opposite ends of the PC1 axis and pTCs were more narrowly grouped around the middle, we found considerable overlap between the three cell types. In summary, the PCA failed to return clear clustering but suggested a more gradual continuum of heterogeneous properties in OB projection neurons.

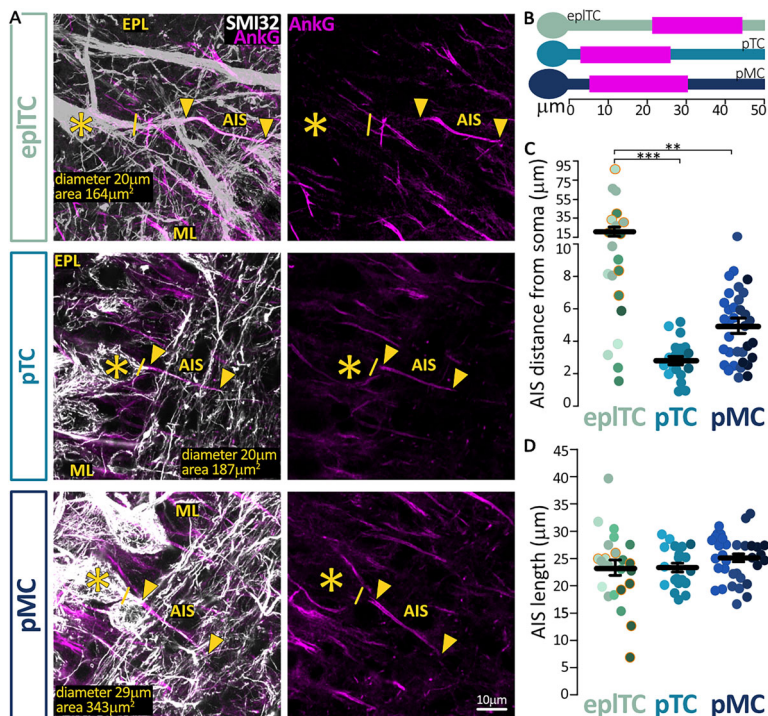


**Figure 5.** EPL cells have similarly long but more distal axon initial segments than ML neurons. **A**, Example maximum intensity projection images of epITC, pTC, and pMC neurons visualized via SMI-32 immunolabel (white) with an identified AnkG-positive AIS (magenta, arrows). The solid line indicates the emergence of the axonal process from the soma (asterisk). EPL, external plexiform layer; ML, mitral layer. **B**, Mean AIS (magenta) start and end position for each group. **C**, **D**, AIS distance from soma and length in epITCs (green,  $n = 23$ ); pTCs (cyan,  $n = 21$ ); and pMCs (blue,  $n = 34$ ). Circles represent individual cells, different color shades represent different mice; orange border indicates AIS originating from dendrite; lines are mean  $\pm$  SEM; \*\* $p < 0.01$ ; \*\*\* $p < 0.001$ .

## Discussion

In this study we compared the morphological and functional properties of ex vivo murine bulbar principal neurons across deep EPL and ML using classification approaches based on often-used soma size threshold and unbiased clustering of membrane capacitance. We were unable to conclusively segregate pMCs and pTCs within the ML, but we confirmed earlier findings that very large ML cells are overall different from TCs in the EPL. Historically, smaller cells in the ML and cells with their soma only partially in the ML have been excluded from analysis because of their ambiguous identity (Burton and Urban, 2014; Nagayama et al., 2014). If these “transitional” cells are ignored, a very clear mitral/tufted split emerges. However, when they are included, such stark classification blurs as summarized by our PCA of AP properties which returned a polarized continuum rather than defined clusters. Taken all together, these data suggest that, besides the often-unavailable connectivity profile, anatomy paired with size and location is still the best classifier of bulbar principal neurons, which are overall extremely heterogeneous.

### Age, recording conditions, and analysis methods strongly influence AP firing

Both ex vivo and in vivo studies have shown that TC cells are more excitable than MCs and that they have a latency to fire in response to OSN inputs (Burton and Urban, 2014). While for 500-ms-long current injections we observed higher numbers of APs in epITC input–output curves, our dataset did not replicate this higher excitability finding when looking more granularly at single AP thresholds. This discrepancy is likely due to both experimental and analysis differences. Indeed, contrary to Burton and Urban (2014), we recorded at lower physiologically relevant temperatures without synaptic blockers in postweaning mice and then normalized the injected shorter-lasting current injections for cell capacitance, which is by definition very different between the groups. Both age and synaptic blockers have been shown to be strong modulators of MC firing (Smithers et al., 2017; Van Hook, 2020; Tufo et al., 2022), which with increasing age becomes more attuned to high-frequency stimuli (Yu et al., 2015) and as such can easily explain the discrepancy. Moreover, our AIS morphological data are in line with the higher firing threshold in epITCs. The AIS location, which together with its morphology has been shown to correlate best with somatic threshold than rheobase, was very distal in epITCs. Given the similar proximal axon diameters in epITCs and ML cells, this suggests that epITCs do not operate in a high coupling regime with the soma and thus need more charge to initiate firing (Brette, 2013; Goethals and Brette, 2020). Furthermore, despite variations in recording conditions, our dataset mirrored the heterogeneity in sag potentials reported previously (Angelo and Margrie, 2011; Burton and Urban, 2014) and in general in most single AP and repetitive firing parameters. When comparing our results with in vivo studies, which primarily used rats of

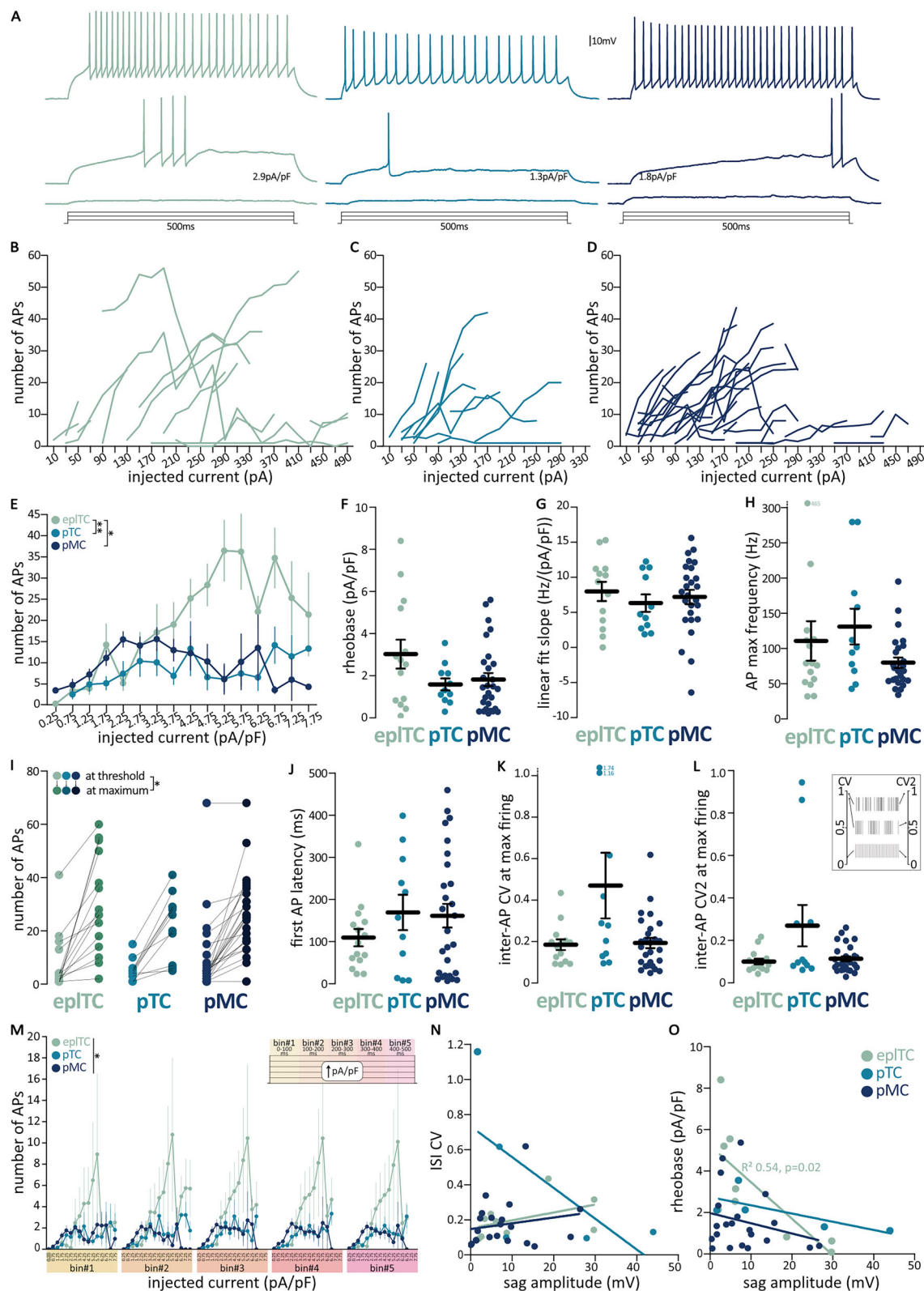


**Figure 6.** Comparable repetitive AP firing among OB projection neurons. **A**, Example traces of the membrane voltage response to 500 ms depolarizing current injections at 300 pA, rheobase, and max AP firing in epITCs (green,  $n = 15$ ); pTCs (cyan,  $n = 11$ ); and pMCs (blue,  $n = 27$ ). **B–D**, Raw input–output plots showing the number of APs fired at each current injection in individual neurons. **E**, Mean number of APs and SEM at each current density (i.e., injected current normalized for cell capacitance) in epITCs (green), pTCs (cyan), and pMCs (blue). Repetitive firing parameters include **(F)** rheobase, **(G)** slope of the number of APs versus current density input–output curves, **(H)** maximum AP firing frequency, **(I)** number of APs at threshold (light shades) and at maximum firing (dark shades), **(J)** latency of the first AP at the current injection level where the max AP number was fired, **(K, L)** CV of the ISIs (CV) and of adjacent ISIs

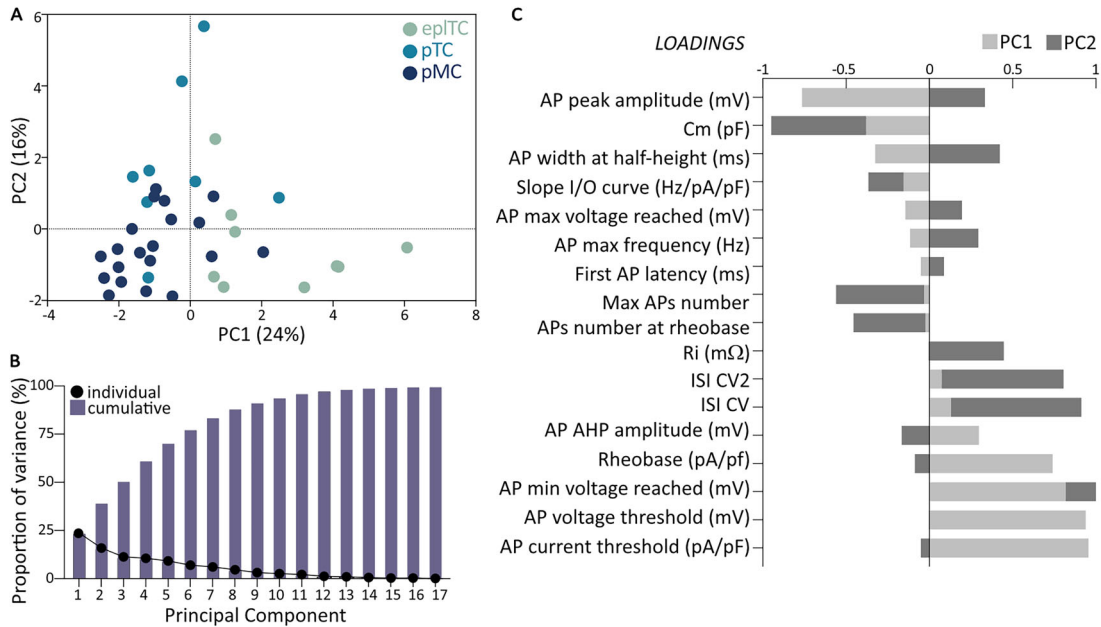


**Figure 7.** PCA of firing properties fails to reveal clear clustering of OB projection neurons. **A**, PC score plot for eplTC (green,  $n = 9$ ) and ML's pTC (cyan,  $n = 8$ ) and pMC (blue,  $n = 20$ ) based on passive properties and all measurements obtained from AP firing recordings (Figs. 2, 4, 6; Table 1). Each circle represents a cell plotted against its primary and secondary PC scores. **B**, Individual (circles) and cumulative (bars) proportion of variance explained by each PC. **C**, Loading scores for all variables showing their respective contributions to PC1 (light gray) and PC2 (dark gray). See also Extended Data Figure 7-1.

various ages as well as transgenic mice, we encountered several challenges. As expected, these studies are highly heterogeneous, with differences in methodology and classifications of MCs and TCs, and none report capacitance (Gang and Isaacson, 2003; Abraham et al., 2010; Phillips et al., 2012). Comparing firing frequency is not feasible due to methodological differences: we induced depolarizing current, while in vivo studies recorded spontaneous firing, which likely accounts for the higher frequencies observed in our study. For instance, Gang and Isaacson (2003) recorded a frequency of  $2.8 \pm 0.7$  Hz in M/TCs, while Phillips et al. (2012) reported  $57.8 \pm 16.9$  Hz. However, our input resistance for pMC ( $110 \pm 13$  MΩ) aligns with the value reported by Gang and Isaacson ( $115.0 \pm 16.0$  MΩ) in young wild-type rats. In summary, while our study is largely consistent with both ex vivo and in vivo work, the differences in experimental approaches, animal models, and ages presented challenges in making direct comparisons.

**Mitral, tufted, and everything in between: gray areas in the classification of bulbar principal neurons**

The cell-to-cell variability within and between putative subclasses that we report here—where we intentionally avoided removing outliers to present the full range of recorded properties—stresses that bulbar principal neurons are a heterogeneous population (Zeppilli et al., 2021). Including both the analysis of the soma size in the fixed tissue and the firing properties, our dataset failed to return a clear separation between pMCs and pTCs in the ML, and even a ML versus deep EPL classification is somewhat blurred. This is not surprising because, while a traditional location + 20-μm-diameter classifier is appealing, there is accumulating evidence of overlap in the molecular and genetic profiles of MCs and TCs. For example, they heterogeneously express GABA<sub>A</sub> receptors and voltage-gated potassium channels (Panzanelli et al., 2005), and while MCs and TCs can be classified at the level of transcriptomics, cell-type-specific modules of gene regulation fail to granularly class MCs and TCs (Zeppilli et al., 2021). Indeed, it is thought that their biophysical diversity is at least partly due not to genetic programs but to experience-dependent factors which have the potential to expand their heterogeneity (Padmanabhan and Urban, 2010; Angelo et al., 2012; Tripathy et al., 2013).

Importantly, OB principal neurons also differ in their morphology of lateral dendrites and their axonal projections and have consequent differences in synaptic connectivity (Christie et al., 2001; Nagayama, 2010; Gire et al., 2012; Nagayama et al., 2014; Geramita et al., 2016; Liu et al., 2019; Imamura et al., 2020; Jones et al., 2020). The combination of structural, functional, intrinsic, and synaptic properties likely returns not two clean groups—MCs and TC—but multiple subgroups (Padmanabhan and Urban, 2010; Angelo and Margrie, 2011; Kikuta et al., 2013; Goillard and Marder, 2021; Zeppilli et al., 2021). This broad diversity could enable the OB to parallelly represent the wide odor and concentration

(CV2; see inset for graphical description) at the current injection level where the max AP number was fired. **M**, Input-output curve with the 500 ms current injection divided into five 100 ms bins (see inset). **N-O**, Correlation of sag amplitude with firing properties. Circles and thin lines are individual cells; thick black lines are mean ± SEM; \* $p < 0.05$ ; \*\* $p < 0.01$ ; further quantification and statistical analysis in Table 1.

space (Lee et al., 2023) via spatially and temporally distributed ensembles of active neurons (Uchida et al., 2014; Geramita et al., 2016; Shmuel et al., 2019).

### Heterogeneity as a key odor processing tool

For most sensory systems, the stimulus space is relatively well known (Huberman and Niell, 2011; King et al., 2015; O'Connor et al., 2021). Conversely, while we have long defined the number colors or sound frequencies mice—or humans—can perceive, the exact size of the olfactory stimulus space remains elusive. What we know is that, given the vast number of potentially detectable chemicals and their nonlinear combinations, the range of odors that animals can detect is truly large (Meister, 2015; Lee et al., 2023). This remarkable capacity is even more remarkable considering that the OSNs continuously regenerate throughout life (Schwob, 2002), a process that raises fascinating questions about how stable perception is maintained despite the constant turnover of the peripheral sensor. Olfactory processing is further unique because it eschews a thalamic relay and information only takes two synapses to go from the nose to cortex and other higher areas (Shepherd, 2004).

Given this stimulus and sensor complexity and such paired down relay anatomy, it is not surprising that the OB needs multiple parallel channels to process odors. It is thus tempting to speculate that heterogeneity of genes, morphologies, intrinsic properties, and synaptic connections is used throughout the olfactory system—principal neurons as well as OSNs and interneurons (Godfrey et al., 2004; Antal et al., 2006; Lledo et al., 2008; Galliano et al., 2018)—to sense, process, and classify olfactory information.

### References

- Abraham NM, et al. (2010) Synaptic inhibition in the olfactory bulb accelerates odor discrimination in mice. *Neuron* 65:399–411.
- Ackels T, Jordan R, Schaefer AT, Fukunaga I (2020) Respiration-locking of olfactory receptor and projection neurons in the mouse olfactory bulb and its modulation by brain state. *Front Cell Neurosci* 14:220.
- Angelo K, Margrie TW (2011) Population diversity and function of hyperpolarization-activated current in olfactory bulb mitral cells. *Sci Rep* 1:50.
- Angelo K, Rancz EA, Pimentel D, Hundahl C, Hannibal J, Fleischmann A, Pichler B, Margrie TW (2012) A biophysical signature of network affiliation and sensory processing in mitral cells. *Nature* 488:375–378.
- Antal M, Eyre M, Finklea B, Nusser Z (2006) External tufted cells in the main olfactory bulb form two distinct subpopulations. *Eur J Neurosci* 24:1124–1136.
- Balu R, Larimer P, Strowbridge BW (2004) Phasic stimuli evoke precisely timed spikes in intermittently discharging mitral cells. *J Neurophysiol* 92:743–753.
- Batista-Brito R, Close J, Machold R, Fishell G (2008) The distinct temporal origins of olfactory bulb interneuron subtypes. *J Neurosci* 28:3966–3975.
- Bender KJ, Trussell LO (2012) The physiology of the axon initial segment. *Annu Rev Neurosci* 35:249–265.
- Boonstra H, Oosterhuis JW, Oosterhuis AM, Fleuren GJ (1983) Cervical tissue shrinkage by formaldehyde fixation, paraffin wax embedding, section cutting and mounting. *Virchows Arch A Pathol Anat Histopathol* 402:195–201.
- Brette R (2013) Sharpness of spike initiation in neurons explained by compartmentalization. *PLoS Comput Biol* 9:e1003338.
- Burton SD, Urban NN (2014) Greater excitability and firing irregularity of tufted cells underlies distinct afferent-evoked activity of olfactory bulb mitral and tufted cells. *J Physiol* 592:2097–2118.
- Cang J, Isaacson JS (2003) In vivo whole-cell recording of odor-evoked synaptic transmission in the rat olfactory bulb. *J Neurosci* 23:4108–4116.
- Cavarretta F, Burton SD, Igarashi KM, Shepherd GM, Hines ML, Migliore M (2018) Parallel odor processing by mitral and middle tufted cells in the olfactory bulb. *Sci Rep* 8:7625.
- Chae H, Banerjee A, Dussauze M, Albeanu DF (2022) Long-range functional loops in the mouse olfactory system and their roles in computing odor identity. *Neuron* 110:3970–3985.e7.
- Christie JM, Schoppa NE, Westbrook GL (2001) Tufted cell dendrodendritic inhibition in the olfactory bulb is dependent on NMDA receptor activity. *J Neurophysiol* 85:169–173.
- Combe CL, Gasparini S (2021) Ih from synapses to networks: HCN channel functions and modulation in neurons. *Prog Biophys Mol Biol* 166:119–132.
- Ezeh PI, Wellis DP, Scott JW (1993) Organization of inhibition in the rat olfactory bulb external plexiform layer. *J Neurophysiol* 70:263–274.
- Fourcaud-Trocmé N, Zbili M, Duchamp-Viret P, Kuczewski N (2022) Afterhyperpolarization promotes the firing of mitral cells through a voltage-dependent modification of action potential threshold. *eNeuro* 9:ENEURO.0401-21.2021.
- Fukunaga I, Berning M, Kollo M, Schmaltz A, Schaefer AT (2012) Two distinct channels of olfactory bulb output. *Neuron* 75:320–329.
- Galliano E, Franzoni E, Breton M, Chand AN, Byrne DJ, Murthy VN, Grubb MS (2018) Embryonic and postnatal neurogenesis produce functionally distinct subclasses of dopaminergic neuron. *eLife* 7:e32373.
- Galliano E, Hahn C, Browne LP, Villamayor PR, Tufo C, Crespo A, Grubb MS (2021) Brief sensory deprivation triggers cell type-specific structural and functional plasticity in olfactory bulb neurons. *J Neurosci* 41:2135–2151.
- Gasser HS, Erlanger J (1929) The role of fiber size in the establishment of a nerve block by pressure or cocaine. *Am J Physiol* 88:581–591.
- Geramita MA, Burton SD, Urban NN (2016) Distinct lateral inhibitory circuits drive parallel processing of sensory information in the mammalian olfactory bulb. *eLife* 5:e16039.
- Gire DH, Franks KM, Zak JD, Tanaka KF, Whitesell JD, Mulligan AA, Hen R, Schoppa NE (2012) Mitral cells in the olfactory bulb are mainly excited through a multistep signaling path. *J Neurosci* 32:2964–2975.
- Goillard J-M, Marder E (2021) Ion channel degeneracy, variability, and covariation in neuron and circuit resilience. *Annu Rev Neurosci* 44:335–357.
- Godfrey PA, Malnic B, Buck LB (2004) The mouse olfactory receptor gene family. *Proc Natl Acad Sci U S A* 101:2156–2161.
- Goethals S, Brette R (2020) Theoretical relation between axon initial segment geometry and excitability. *eLife* 9:e53432.
- Goldfarb M, et al. (2007) Fibroblast growth factor homologous factors control neuronal excitability through modulation of voltage-gated sodium channels. *Neuron* 55:449–463.
- Hamada MS, Goethals S, de Vries SI, Brette R, Kole MHP (2016) Covariation of axon initial segment location and dendritic tree normalizes the somatic action potential. *Proc Natl Acad Sci U S A* 113:14841–14846.

- Hodapp A, et al. (2022) Dendritic axon origin enables information gating by perisomatic inhibition in pyramidal neurons. *Science* 377:1448–1452.
- Holt GR, Softky WR, Koch C, Douglas RJ (1996) Comparison of discharge variability in vitro and in vivo in cat visual cortex neurons. *J Neurophysiol* 75:1806–1814.
- Hubel DH, Wiesel TN (1959) Receptive fields of single neurones in the cat's striate cortex. *J Physiol* 148:574–591.
- Huberman AD, Niell CM (2011) What can mice tell us about how vision works? *Trends Neurosci* 34:464–473.
- Igarashi KM, et al. (2012) Parallel mitral and tufted cell pathways route distinct odor information to different targets in the olfactory cortex. *J Neurosci* 32:7970–7985.
- Imamura F, Ito A, LaFever BJ (2020) Subpopulations of projection neurons in the olfactory bulb. *Front Neural Circuits* 14:561822.
- Jones S, Zylberberg J, Schoppa N (2020) Cellular and synaptic mechanisms that differentiate mitral cells and superficial tufted cells into parallel output channels in the olfactory bulb. *Front Cell Neurosci* 14:614377.
- Kikuta S, Fletcher ML, Homma R, Yamasoba T, Nagayama S (2013) Odorant response properties of individual neurons in an olfactory glomerular module. *Neuron* 77:1122–1135.
- King J, Insanally M, Jin M, Martins ARO, D'amour JA, Froemke RC (2015) Rodent auditory perception: critical band limitations and plasticity. *Neuroscience* 296:55–65.
- Kishi K, Mori K, Ojima H (1984) Distribution of local axon collaterals of mitral, displaced mitral, and tufted cells in the rabbit olfactory bulb. *J Comp Neurol* 225:511–526.
- Koldaeva A, Zhang C, Huang Y-P, Reinert JK, Mizuno S, Sugiyama F, Takahashi S, Soliman T, Matsunami H, Fukunaga I (2021) Generation and characterization of a cell type-specific, inducible Cre-driver line to study olfactory processing. *J Neurosci* 41:6449–6467.
- Kole MHP, Letzkus JJ, Stuart GJ (2007) Axon initial segment Kv1 channels control axonal action potential waveform and synaptic efficacy. *Neuron* 55:633–647.
- Lee BK, et al. (2023) A principal odor map unifies diverse tasks in olfactory perception. *Science* 381:999–1006.
- Leterrier C (2018) The axon initial segment: an updated viewpoint. *J Neurosci* 38:2135–2145.
- Liu G, et al. (2019) Target specific functions of EPL interneurons in olfactory circuits. *Nat Commun* 10:3369.
- Lledo P-M, Merkle FT, Alvarez-Buylla A (2008) Origin and function of olfactory bulb interneuron diversity. *Trends Neurosci* 31:392–400.
- Ma J, Dankulich-Nagrudny L, Lowe G (2013) Cholecystokinin: an excitatory modulator of mitral/tufted cells in the mouse olfactory bulb. *PLoS One* 8:e64170.
- Meister M (2015) On the dimensionality of odor space. *eLife* 4:e07865.
- Mori K, Kishi K, Ojima H (1983) Distribution of dendrites of mitral, displaced mitral, tufted, and granule cells in the rabbit olfactory bulb. *J Comp Neurol* 219:339–355.
- Nagai Y, Sano H, Yokoi M (2005) Transgenic expression of Cre recombinase in mitral/tufted cells of the olfactory bulb. *Genes* 43:12–16.
- Nagayama S (2010) Differential axonal projection of mitral and tufted cells in the mouse main olfactory system. *Front Neural Circuits* 4:120.
- Nagayama S, Homma R, Imamura F (2014) Neuronal organization of olfactory bulb circuits. *Front Neural Circuits* 8:98.
- Nagayama S, Takahashi YK, Yoshihara Y, Mori K (2004) Mitral and tufted cells differ in the decoding manner of odor maps in the rat olfactory bulb. *J Neurophysiol* 91:2532–2540.
- Nakajima D, Nakayama M, Kikuno R, Hirosawa M, Nagase T, Ohara O (2001) Identification of three novel non-classical cadherin genes through comprehensive analysis of large cDNAs. *Brain Res Mol Brain Res* 94:85–95.
- Nassi JJ, Callaway EM (2009) Parallel processing strategies of the primate visual system. *Nat Rev Neurosci* 10:360–372.
- O'Connor DH, Krubitzer L, Bensmaia S (2021) Of mice and monkeys: somatosensory processing in two prominent animal models. *Prog Neurobiol* 201:102008.
- Orona E, Rainer EC, Scott JW (1984) Dendritic and axonal organization of mitral and tufted cells in the rat olfactory bulb. *J Comp Neurol* 226:346–356.
- Padmanabhan K, Urban NN (2010) Intrinsic biophysical diversity decorrelates neuronal firing while increasing information content. *Nat Neurosci* 13:1276–1282.
- Panzanelli P, Perazzini A-Z, Fritschy J-M, Sassoè-Pognetto M (2005) Heterogeneity of  $\gamma$ -aminobutyric acid type a receptors in mitral and tufted cells of the rat main olfactory bulb. *J Comp Neurol* 484:121–131.
- Phillips ME, Sachdev RNS, Willhite DC, Shepherd GM (2012) Respiration drives network activity and modulates synaptic and circuit processing of lateral inhibition in the olfactory bulb. *J Neurosci* 32:85–98.
- Pinching AJ, Powell TP (1971) The neuropil of the periglomerular region of the olfactory bulb. *J Cell Sci* 9:379–409.
- Royet JP, Distel H, Hudson R, Gervais R (1998) A re-estimation of the number of glomeruli and mitral cells in the olfactory bulb of rabbit. *Brain Res* 788:35–42.
- Schneider SP, Macrides F (1978) Laminar distributions of interneurons in the main olfactory bulb of the adult hamster. *Brain Res Bull* 3:73–82.
- Schwob JE (2002) Neural regeneration and the peripheral olfactory system. *Anat Rec* 269:33–49.
- Shepherd GM (2004) *The synaptic organization of the brain*, Ed 5th. Oxford, New York: Oxford University Press.
- Shmuel R, Secundo L, Haddad R (2019) Strong, weak and neuron type dependent lateral inhibition in the olfactory bulb. *Sci Rep* 9:1602.
- Smithers HE, Terry JR, Brown JT, Randall AD (2017) Aging-associated changes to intrinsic neuronal excitability in the bed nucleus of the stria terminalis is cell type-dependent. *Front Aging Neurosci* 9:424.
- Tripathy SJ, Padmanabhan K, Gerkin RC, Urban NN (2013) Intermediate intrinsic diversity enhances neural population coding. *Proc Natl Acad Sci U S A* 110:8248–8253.
- Tufo C, Poopalasundaram S, Dorrego-Rivas A, Ford MC, Graham A, Grubb MS (2022) Development of the mammalian main olfactory bulb. *Development* 149:dev200210.
- Uchida N, Poo C, Haddad R (2014) Coding and transformations in the olfactory system. *Annu Rev Neurosci* 37:363–385.
- Van Hook MJ (2020) Temperature effects on synaptic transmission and neuronal function in the visual thalamus. *PLoS One* 15:e0232451.
- Yamada R, Kuba H (2016) Structural and functional plasticity at the axon initial segment. *Front Cell Neurosci* 10:250.
- Yu Y, Burton SD, Tripathy SJ, Urban NN (2015) Postnatal development attunes olfactory bulb mitral cells to high-frequency signaling. *J Neurophysiol* 114:2830–2842.
- Zeppilli S, Ackels T, Attey R, Klimpert N, Ritola KD, Boeing S, Crombach A, Schaefer AT, Fleischmann A (2021) Molecular characterization of projection neuron subtypes in the mouse olfactory bulb. *eLife* 10:e65445.